

# Inter-Calibration of Microwave Radiometers Using the Vicarious Cold Calibration Double Difference Method

Rachael A. Kroodsma, *Student Member, IEEE*, Darren S. McKague, *Member, IEEE*, and  
Christopher S. Ruf, *Fellow, IEEE*

**Abstract**—The double difference method of inter-calibration between spaceborne microwave radiometers is combined with the vicarious cold calibration method for calibrating an individual radiometer. Vicarious cold calibration minimizes the effects of geophysical variability on radiative transfer models (RTMs) of the brightness temperature (TB) data and it accounts for frequency and incidence angle dissimilarity between radiometers. Double differencing reduces the sensitivity of the inter-calibration to RTM error and improper accounting for geophysical variables in the RTM. When combined together, the two methods significantly improve the confidence with which calibration differences can be identified and characterized. This paper analyzes the performance of the vicarious cold calibration double difference method for conical scanning microwave radiometers and quantifies the improvement this method provides compared to performing a simpler inter-calibration by direct comparison of radiometer measurements.

**Index Terms**—Calibration, microwave radiometry.

## I. INTRODUCTION

**A**N ACCURATE inter-calibration of microwave radiometers is necessary if data from several different radiometers are to be compared. One of the useful applications of inter-calibration is to provide long-term climate data records, since the lifetime of a single satellite is not long enough to produce these records. There are now readily available data from many microwave radiometers dating back several decades that can be used for climate studies. Having the ability to inter-calibrate these data will enable more accurate climate data records than just using single satellites without inter-comparing them.

One natural candidate for inter-calibration is the series of Special Sensor Microwave/Imager (SSM/I) radiometers. The first SSM/I was launched in 1987 and since then there have been many efforts to combine data from the various SSM/I

platforms over the years into a cohesive data set [1]–[3]. One advantage of inter-calibrating data from identical instruments on different platforms is that the center frequencies are the same. However, a major disadvantage of inter-calibrating SSM/I data is that the instruments all fly on sun-synchronous satellites with different equatorial crossing times. Yan [3] uses a method for inter-calibration that relies on finding cross-over points between the different platforms, which only occur near the poles for sun-synchronous orbiters. This greatly limits the amount of available data that can be used for inter-calibration. Inter-calibrating a sun-synchronous orbiter with a radiometer in a non-sun-synchronous, low inclination orbit, as was done by Wentz [4] creates a larger potential data set of cross-over points. Wentz uses the Tropical Rainfall Measuring Mission (TRMM) Microwave Imager (TMI) along with various SSM/I platforms and performs an inter-calibration between TMI and SSM/I. While the number of potential data points is increased using this approach, it still restricts the inter-comparison to cross-over points only. The inter-calibration method presented here does not require cross-over points between satellites and therefore has the advantage that it can be used to compare any two radiometers, regardless of their orbits.

In order to inter-calibrate two microwave radiometers, individual instrument characteristics have to be taken into account. These characteristics include center frequency, bandwidth, earth incidence angle (EIA), and orbital characteristics such as altitude and orbital inclination. Typical microwave radiometer imagers that are used for atmospheric and surface remote sensing have similar channels, but vary slightly in frequency and EIA. Table I shows the frequencies, EIAs, and orbital characteristics of four current spaceborne conical scanning microwave radiometers. Only low resolution channels are shown.

One key application of the vicarious cold calibration double difference method is the upcoming Global Precipitation Measurement (GPM) mission. GPM is an international multi-satellite mission that will measure precipitation from space [9]. The GPM mission is unique in that it will utilize several different microwave radiometers on individual satellites to provide global coverage of precipitation measurements. Inter-calibration of the radiometers is a key aspect of the mission, intended to ensure that consistent measurements are made among the radiometers in the constellation. The Inter-Calibration Working Group (X-Cal) is responsible for developing algorithms for inter-calibrating the radiometers included in GPM [10]–[12]. The group is using radiometer data from the

Manuscript received September 30, 2011; revised January 19, 2012; accepted March 04, 2012. Date of publication May 30, 2012; date of current version June 28, 2012. This work was supported in part by NASA Grant NNX10AM12H.

R. A. Kroodsma is with the Department of Atmospheric, Oceanic, and Space Sciences, University of Michigan, Ann Arbor, MI 48109 USA (corresponding author, e-mail: rakro@umich.edu).

D. S. McKague is with the Department of Atmospheric, Oceanic, and Space Sciences, University of Michigan, Ann Arbor, MI 48109 USA (e-mail: dmckague@umich.edu).

C. S. Ruf is with the Space Physics Research Laboratory, Department of Atmospheric, Oceanic, and Space Sciences, University of Michigan, Ann Arbor, MI 48109 USA (e-mail: cruf@umich.edu).

Color versions of one or more of the figures in this paper are available online at <http://ieeexplore.ieee.org>.

Digital Object Identifier 10.1109/JSTARS.2012.2195773

TABLE I  
FREQUENCIES, EIAs, AND ORBITAL CHARACTERISTICS OF FOUR CURRENT SPACEBORNE MICROWAVE RADIOMETERS [5]–[8]

Radiometer	Frequency (GHz)					Nominal EIA (degrees)	Orbital Altitude (km)	Orbital Inclination (degrees)
	6.8V 6.8H	10.7V 10.7H	18.7V 18.7H	23.8V 23.8H	37.0V 37.0H			
WindSat	6.8V 6.8H	10.7V 10.7H	18.7V 18.7H	23.8V 23.8H	37.0V 37.0H	49.9-55.3	840	98.7
TMI		10.65V 10.65H	19.35V 19.35H	21.3V	37.0V 37.0H	53.3 (post-boost)	402.5 (post-boost)	35
AMSR-E	6.925V 6.925H	10.65V 10.65H	18.7V 18.7H	23.8V 23.8H	36.5V 36.5H	55	705	98
SSM/I			19.35V 19.35H	22.235V	37.0V 37.0H	53.1	833	98.8

year July 2005–June 2006 to develop these algorithms. Two of the radiometers currently under study for that time period are TMI and the Advanced Microwave Scanning Radiometer (AMSR-E). These radiometers are used as examples in this study.

## II. INTER-CALIBRATION ALGORITHM

The inter-calibration algorithm presented in this paper makes use of the double difference method. The double difference provides a way to inter-calibrate two microwave radiometers that accounts for frequency, EIA, and orbital differences between platforms. To calculate the double difference, the single differences for each radiometer are first computed. The single difference is found by taking the difference between a reference statistic of the observed radiometer brightness temperatures (TBs) and a reference statistic from simulated TBs. The double difference is then the difference between the single differences of the two radiometers being inter-calibrated. This paper will explore how well the double difference method is able to remove geophysical variability and account for known radiometer differences for the inter-calibration of microwave radiometers.

This method of inter-calibration is demonstrated using the vicarious cold calibration [13]. The vicarious cold calibration uses the theory that the coldest TBs that a microwave radiometer observes are over the ocean with calm surface winds, no clouds, and minimal water vapor. The single difference makes use of this cold reference TB calculated from a radiometer's observations and compares it to a cold reference TB calculated from simulations. These simulations are top of atmosphere (TOA) TBs that are generated using a radiative transfer model (RTM) with inputs from the Global Data Assimilation System (GDAS) [14]. Since the coldest TBs occur for calm ocean with no clouds and minimal water vapor, these conditions are relatively straightforward to simulate with an RTM that accounts for atmospheric absorption. The TOA TB is calculated according to

$$TB_{TOA} = TB_{up} + \left[ \varepsilon_s(f, \theta) T_s + (1 - \varepsilon_s(f, \theta)) \times (TB_{dn} + T_c e^{-\tau(f) \sec \theta}) \right] e^{-\tau(f) \sec \theta} \quad (1)$$

where the optical depth  $\tau$  is given by

$$\tau(f) = \int_0^{TOA} \alpha(f, z) dz \quad (2)$$

and the upwelling ( $TB_{up}$ ) and downwelling ( $TB_{dn}$ ) brightness temperatures are given by

$$TB_{up} = \sec \theta \int_0^{TOA} \alpha(f, z) T(z) \times \exp \left( - \sec \theta \int_0^{TOA} \alpha(f, z') dz' \right) dz \quad (3)$$

$$TB_{dn} = \sec \theta \int_0^{\infty} \alpha(f, z) T(z) \times \exp \left( - \sec \theta \int_0^z \alpha(f, z') dz' \right) dz \quad (4)$$

$TB_{up}$  and  $TB_{dn}$  are functions of the frequency  $f$ , earth incidence angle  $\theta$ , absorption coefficient profile  $\alpha(f, z)$ , and the temperature profile  $T(z)$ . The TOA TB is then calculated from  $TB_{up}$ ,  $TB_{dn}$ , the surface emissivity  $\varepsilon_s(f, \theta)$ , surface temperature  $T_s$ , the cosmic background temperature  $T_c$ , and the optical depth  $\tau$ . The surface emissivity is a function of frequency and EIA, and the optical depth is a function of frequency. The surface emissivity is found using a combination of models that includes the Meissner and Wentz dielectric constant model [15], along with the Hollinger surface roughness [16], Stogryn foam [17], Wilheit wind speed [18], and Elsaessar surface [19] models. Although the vicarious cold cal algorithm finds the coldest TBs that occur with calm winds, it is still necessary to have a surface emissivity model that accounts for wind. This is because the vicarious cold cal TB is found by extrapolating to the coldest TB point using slightly warmer TBs that might include surface wind effects. The effect of wind direction on emissivity is ignored here. This should only be a small error since this error scales with wind [20] and the vicarious cold cal algorithm uses only TB data with light wind. Absorption in the atmosphere is accounted for with the Rosencrantz 1998 model for water vapor [21], the Liebe 1991 model for liquid water [22], and the Liebe 1992 model for oxygen absorption [23].

The inputs from GDAS include atmospheric and surface parameters such as sea surface temperature (SST), surface wind speed, and profiles of temperature and relative humidity. These parameters are given every six hours over the entire globe at  $1^\circ$  latitude/longitude intervals. The simulated TBs from the RTM are created using the center frequencies, polarization, and EIAs that correspond to the radiometer of interest using the closest grid point in space and time.

The cold cal TB is computed from histograms of the TB population for a given time period and geographic region. For this

study, the radiometer TB data are sampled by month, hemisphere (Northern and Southern), and orbit (ascending and descending). Only data over ocean are used as inputs to the cold cal algorithm, so a land flag and ice flag taken from GDAS are used to filter the TBs. The quality flag given in the radiometer data is also used to filter the TBs. The TBs are then binned into histograms that are input to the vicarious cold cal algorithm. Since the vicarious cold cal algorithm is based on an unbiased statistical estimator, the number of TB samples in the histogram does not change the expected value of the cold cal TB, only the uncertainty. To minimize this uncertainty, the TBs from an entire month of radiometer data are used rather than a shorter time period. Also, since the location of the cold cal TB can change seasonally as well as over time due to SST and water vapor fluctuations, an entire hemisphere of TB data is input to the cold cal algorithm. This ensures that the coldest TBs are input to the vicarious cold cal algorithm. Details concerning how the vicarious cold cal TB is computed from the histograms are given in [13].

The vicarious cold cal TB ( $TB_{cold}$ ) is computed for both the observations and simulations, and the difference between these values is found. This yields the vicarious cold calibration single difference. Given the single differences for two radiometers A and B, the double difference (DD) can be computed from the difference of these two single differences according to

$$DD = (TB_{cold}^{A,obs} - TB_{cold}^{A,sims}) - (TB_{cold}^{B,obs} - TB_{cold}^{B,sims}) \quad (5)$$

One advantage that the cold calibration double difference method has over other methods of inter-calibration is that it does not require coincident or near-coincident cross-over points between the two radiometers. As will be shown, diurnal variability only has a small effect on the cold cal TB when comparing two radiometers with different observation times. The simulated TBs are able to model the variability in the observed TBs, creating a stationary statistic through the single difference. It is therefore not necessary to match the data by time when comparing one radiometer to another with the double difference method. Another advantage of the cold calibration double difference method is that it is less sensitive to errors in the RTM and modeled atmosphere inputs (GDAS in this case). For example, if the surface emissivity model has an error associated with calculating the contribution of surface wind to the emissivity, this error would be smallest with light wind, which is what the cold cal algorithm uses. Also, the cold cal algorithm uses data where the atmospheric contribution to TB is minimal, so this decreases the error associated with the absorption model as well as the water vapor and cloud liquid water fields provided by GDAS.

A flow diagram of the vicarious cold calibration double difference processing is shown in Fig. 1.

### III. PERFORMANCE OF INTER-CALIBRATION ALGORITHM

An analysis of the inter-calibration algorithm is presented by examining the variations over one year in the observed cold cal TB, single difference, and double difference. The observed cold cal TB and single difference are shown using data from AMSR-E, and the double difference is shown with data from

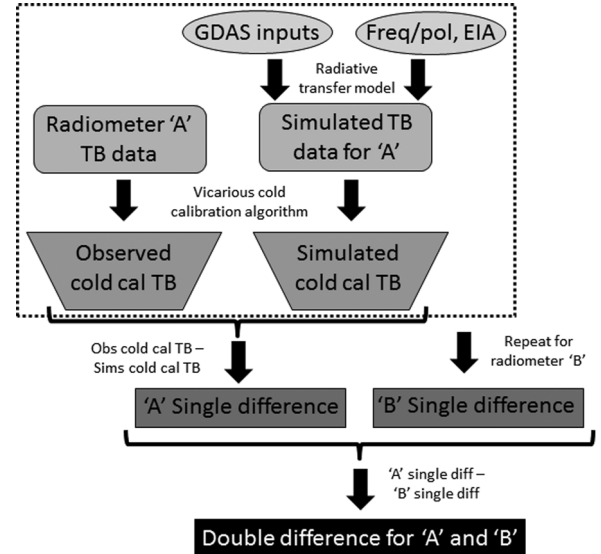


Fig. 1. Flow diagram of the vicarious cold calibration double difference algorithm.

AMSR-E and TMI. The TBs are sampled monthly and regionally over the globe. The vicarious cold calibration algorithm is used to find the cold cal TB for each month and region. For purposes of evaluating instrument calibration biases, the presence of a seasonal cycle in the inter-calibration is undesirable. One way to quantify the seasonal variation in the cold cal TB is to take the difference between the yearly maximum and minimum cold cal TB values, i.e., the amplitude of the seasonal cycle. The greater this difference, the more poorly natural geophysical variability has been accounted for. The amplitude of the annual cycle provides a performance metric that characterizes one important property of an inter-calibration method.

#### A. Observed Cold Cal TB

The cold cal TBs are derived from clear sky, calm ocean scenes. Therefore, the dominant source of geophysical variability in this TB population comes from water vapor. Water vapor in the atmosphere naturally fluctuates throughout the year due to seasonal changes. While the cold calibration algorithm minimizes the impact of water vapor, it does not completely eliminate it. This shows up most readily on the water vapor channels of microwave radiometers. Fig. 2 gives an example of how the observed cold cal TB changes over a year for the AMSR-E 23.8 GHz vertically polarized (V-pol) channel. Fig. 2 shows the cold cal TB sampled in three regions: the Northern Hemisphere (NH), the Southern Hemisphere (SH), and the globe (both NH and SH). Each point in the figure represents a cold cal TB point calculated using one month of data. The amplitude of the seasonal cycle for the globe, the NH, and the SH cold cal TB is 1.73 K, 9.70 K, and 1.92 K, respectively. The NH clearly has a very strong water vapor seasonal cycle compared to the SH.

Fig. 3 shows the same data sample as Fig. 2 only for AMSR-E 10.65 V GHz. The 23.8 GHz channel of AMSR-E has the greatest sensitivity to water vapor, and the 10.65 GHz channel has the least. However, there is still a seasonal cycle

TABLE II  
SUMMARY OF RESULTS FOR THE OBSERVED COLD CAL TB AND SINGLE DIFFERENCE SEASONAL CYCLE AMPLITUDE. THE SINGLE DIFFERENCE HAS A SMALLER SEASONAL CYCLE AMPLITUDE THAN THE OBSERVED COLD CAL TB

Seasonal cycle amplitude (K)		Globe	NH	SH
AMSR-E 10.65V GHz	<b>Observed cold cal TB</b>	0.73	2.13	0.75
	<b>Single Difference</b>	0.43	0.94	0.56
AMSR-E 23.8V GHz	<b>Observed cold cal TB</b>	1.73	9.70	1.92
	<b>Single Difference</b>	0.57	0.63	0.79

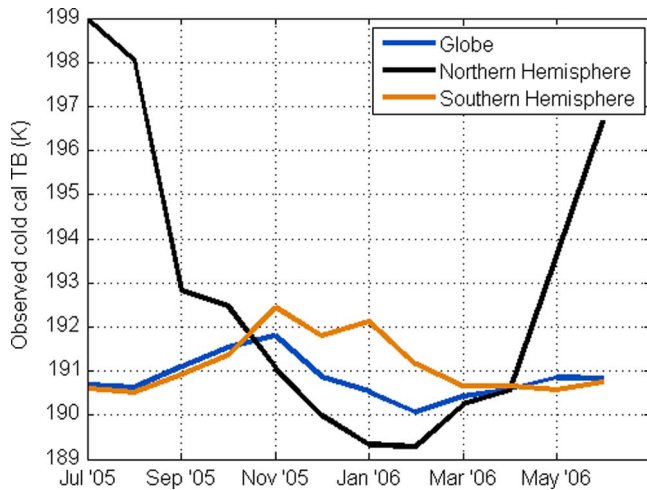


Fig. 2. AMSR-E 23.8 V GHz observed cold cal TB over a year for the globe, NH, and SH. The NH cold cal TB shows a strong seasonal cycle, which is attributed to the large variation in water vapor throughout the year.

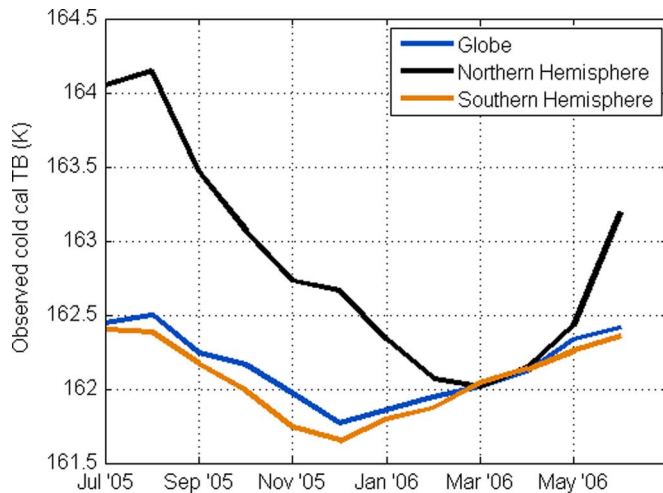


Fig. 3. AMSR-E 10.65 V GHz observed cold cal TB over a year for the globe, NH, and SH. This channel has a smaller seasonal cycle than 23.8 GHz since it is not as sensitive to atmospheric water vapor.

that needs to be removed so that it is not included in the inter-calibration. This small seasonal cycle could be due to variations in SST, since the TB at 10.65 GHz is more sensitive to SST than at higher frequencies. For this channel, the amplitude for the globe, the NH, and the SH cold cal TB seasonal cycle is 0.73 K, 2.13 K, and 0.75 K, respectively.

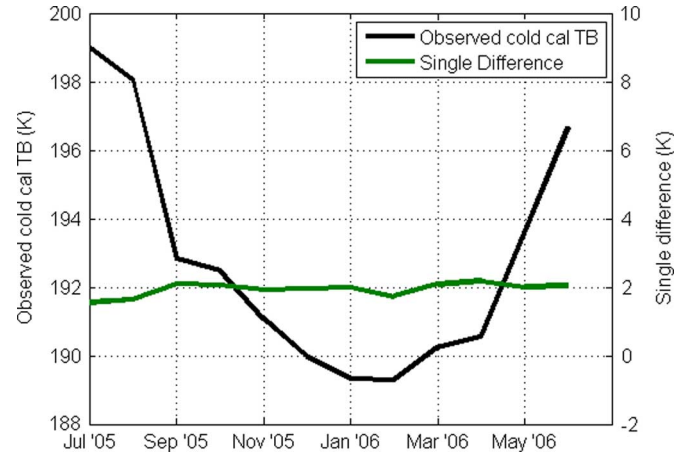


Fig. 4. Comparison of AMSR-E observed cold cal TB and the single difference for the NH. The simulated TBs are able to model the geophysical variability and reduce the seasonal cycle.

### B. Single Difference

In order to minimize the seasonal variability in the cold cal TB, the single difference is used. Fig. 4 gives an example of this by showing the value of the single difference and cold cal TB over one year. The data are from AMSR-E 23.8 V GHz observations and simulations for just the NH since the NH displays the most seasonal variability. The seasonal cycle amplitude for the observed cold cal TB is 9.70 K, while for the single difference the amplitude is reduced to 0.63 K.

Table II summarizes the results for the single difference and observed cold cal seasonal cycle amplitudes. For comparison, both AMSR-E 10.65 V and 23.8 V GHz channels are given for the globe, NH, and SH. In all cases, the single difference reduces the seasonal cycle in the observed cold cal TB. For example, the AMSR-E 23.8 V channel displays a 1.73 K seasonal cycle amplitude in the observed cold cal TB for the globe. The inclusion of the simulated TBs in the single difference decreases this amplitude to 0.57 K.

Since the cold cal TB also varies as a function of EIA, the single difference needs to be able to remove any EIA variation in the radiometer data. One way to see the dependence on EIA is to look at the cold cal TB across the scan. AMSR-E and TMI are both conical scanning radiometers, and EIAs can vary across the scan if there is a satellite attitude offset in roll and pitch. Deviation from the nominal EIA impacts the cold cal TB [24], so it is important to be able to model this in the simulations. Fig. 5 shows the dependence of EIA on scan position for AMSR-E

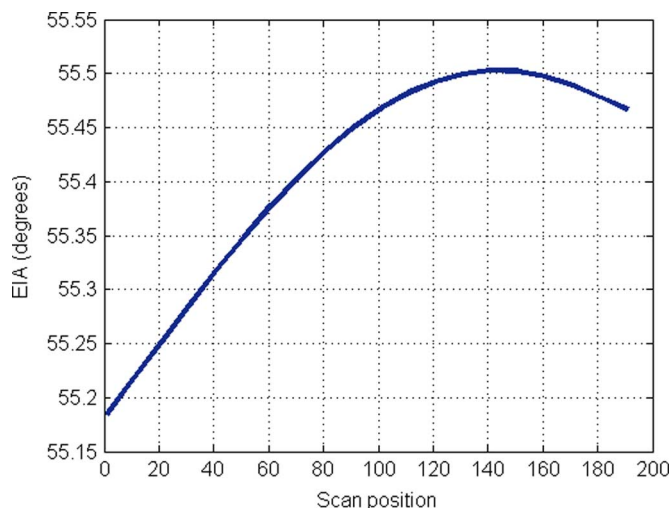


Fig. 5. Scan dependent EIAs for AMSR-E SH descending orbits. The EIA is the same for all low resolution AMSR-E frequencies and polarizations.

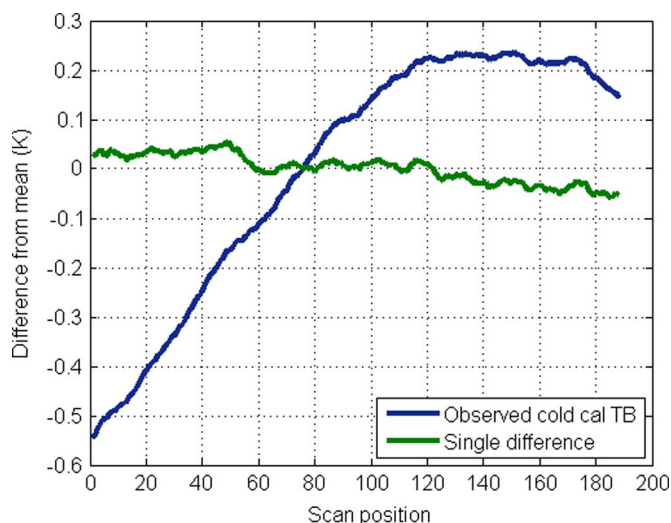


Fig. 6. Observed cold cal TB and single difference across the scan for AMSR-E 10.65 V SH descending orbits. The simulations are able to model the EIA variation across the scan and reduce the variation for the single difference.

Southern Hemisphere descending orbits. The EIAs are given in the radiometer data for each scan position as well as for each scan line, since the EIAs can also change throughout the orbit due to the oblateness of the Earth or eccentricity in the satellite orbit.

For V-pol channels, the cold cal TB changes by approximately 2 K for every 1 degree change in EIA. Fig. 6 demonstrates this effect of EIA variability on the observed cold cal TB as well as the ability of the single difference to remove it for the AMSR-E 10.65 V GHz channel. The 10.65 GHz frequency is chosen in order to have minimal TB contribution from the atmosphere and V-pol is selected to minimize the effect of surface roughness from wind. Therefore, the main influence on the cold cal TB should just be EIA. The observed cold cal TB and single difference are plotted as a running average over nine scan positions to reduce the noise. Also, the TBs are limited to SH descending orbits only since the across-scan EIA variability is at a maximum for these orbits. This analysis also works for the

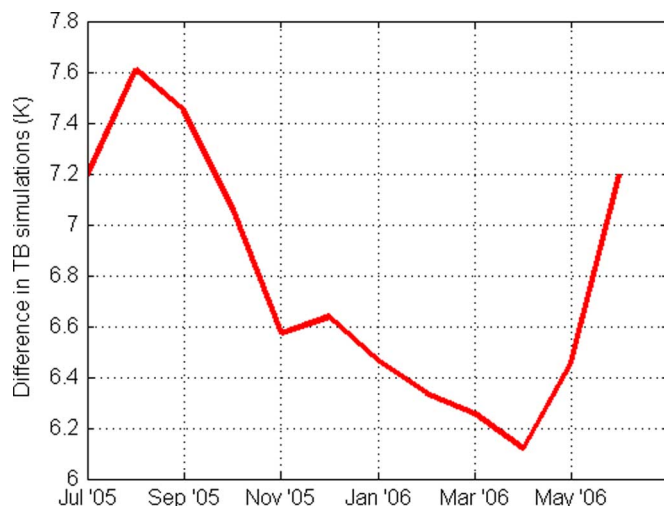


Fig. 7. TB difference between RTM simulations of AMSR-E and TMI by month for the 22 V channel. This discrepancy associated with performing the direct comparison can be attributed to the frequency and EIA differences of AMSR-E and TMI.

NH and ascending orbits since the radiometer data gives EIAs throughout the orbit. The single difference shows that the simulations are able to model the observations and reduce the effect of EIA variation on the cold cal TB to approximately 0.1 K.

### C. Direct Comparison Method

A simple method for inter-calibration involves directly comparing the observations of one radiometer with another. Using the vicarious cold calibration, the direct comparison is just the difference between the observed cold cal TBs of two radiometers. This eliminates the need for simulating TBs through an RTM, but the large TB difference associated with not including the simulations is too great to ignore. Especially for a mission such as GPM that involves comparing radiometers with different frequencies and EIAs, the simulations are a critical part of the inter-calibration method. Even if the two radiometers being compared have the same center frequency and nominal EIA (e.g., two SSM/I radiometers), there could be small attitude offsets of the satellite that will cause slightly different EIAs for each platform. Also, if the equatorial crossing times are different for each platform, the simulated TBs can account for diurnal variability in the manner shown above for seasonal variability.

The discrepancy between performing the direct comparison for AMSR-E and TMI versus the double difference can be quantified by taking the difference between the simulations for each radiometer. Fig. 7 shows this discrepancy, by month, for 22 V. Two likely contributors to this are the difference in water vapor channels between AMSR-E and TMI and the difference in orbits. AMSR-E's water vapor channel is 23.8 GHz with a nominal EIA of  $55^\circ$ , while TMI's water vapor channel is 21.3 GHz with a nominal EIA of  $53.3^\circ$ . To determine what part of this difference is associated with frequency, EIA, or orbital differences, the simulations are run holding two of those variables constant while varying the other one. For example, to determine the contribution due to frequency differences, the simulations are run at 21.3 GHz and 23.8 GHz, while keeping the same nominal EIA

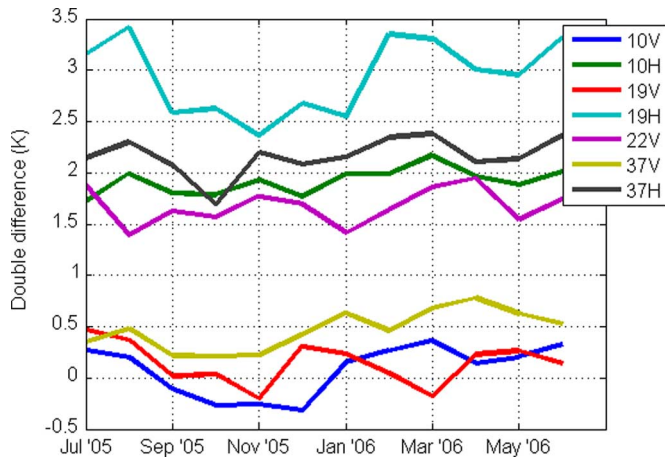


Fig. 8. Double difference by month and channel for AMSR-E and TMI.

and orbit. The difference in frequency contributes about 4 K to the direct comparison and the EIA difference approximately 3 K. The contribution to the direct comparison TB from differences in observation time caused by orbital differences (in this case a low inclination orbiter compared with a sun-synchronous orbiter) is only a few tenths of a Kelvin. This shows that diurnal variability has a very small effect on the cold cal TB, since the observation times of the two radiometers contribute little to the direct comparison TB. These frequency, EIA, and orbital difference values for the 22 V channel are the largest differences in the simulations of all seven inter-calibration channels.

#### D. Double Difference Method

The double difference is an improvement over the direct comparison due to the inclusion of the simulated TBs through the single difference. Once the single difference has been used to minimize geophysical and EIA effects in the cold cal TB, the double difference can be used to calculate the calibration difference between two radiometers. As an example of this, the double difference algorithm is performed on the year of data for AMSR-E and TMI. The result of this by month for each channel is shown in Fig. 8. The double difference is calculated as AMSR-E minus TMI. This is the calibration difference between the two radiometers that results from instrument design differences.

It is also noteworthy that the quality of the double difference is significantly improved when the AMSR-E data are filtered to match the same latitudes as are observed by TMI. TMI only observes latitudes up to about  $\pm 40^\circ$  due to its low inclination orbit, while the AMSR-E inclination provides global coverage. The AMSR-E single difference using data from all latitudes does not have an apparent seasonal cycle. However, the TMI single difference for the water vapor channel does have a seasonal cycle. The AMSR-E and TMI single differences for 22 V are shown in Fig. 9. One hypothesis for this discrepancy is that the GDAS inputs to the RTM, especially the water vapor burden, are not an accurate representation of reality. Therefore, the simulated TBs are not able to exactly model the geophysical variability in the observed cold cal TB. This causes a problem for TMI due to its TB population being limited to the tropics where the water vapor

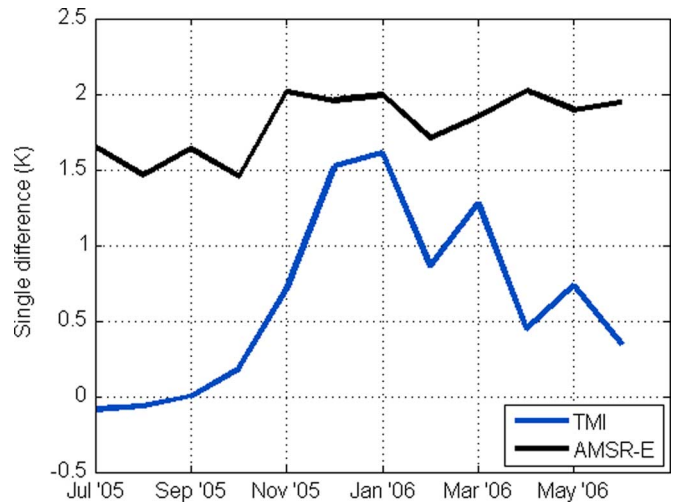


Fig. 9. Single difference for 22 V channel by month for TMI and AMSR-E. AMSR-E single difference doesn't appear to have a seasonal cycle while TMI has a very apparent cycle.

burden is greatest and varies the most. AMSR-E's TB population includes the whole globe, so it is able to find the coldest TBs that lie outside  $\pm 40^\circ$  where the water vapor is minimal and the simulations are better able to model the observations.

Using the global TB population for AMSR-E results in a minimal seasonal cycle. However, if this single difference is used with the TMI single difference, the result is an undesirable seasonal cycle in the double difference. This presents the problem that either the TMI simulations need to be improved, or the AMSR-E single difference needs to be modified to model the trend of the TMI single difference. When the AMSR-E data are filtered to match the latitudes observed by TMI, the result is a seasonal cycle in the AMSR-E single difference that closely matches the TMI single difference trend, as seen in Fig. 10. This improves the quality of the double difference, as seen in Fig. 11. Limiting the latitudes of AMSR-E reduces the seasonal cycle in the double difference for the 22 V channel to less than 0.6 K.

Table III gives a comparison between the amplitude of the seasonal cycle in the double difference found by limiting AMSR-E latitudes versus keeping all the data. In every channel the double difference calculated by limiting the AMSR-E latitudes has a smaller seasonal cycle amplitude. The premise of the double difference is that it should be able to reduce any potential errors in the simulations, e.g., the water vapor fields not being accurate. However, this analysis shows that the double difference is only able to account for those errors if the radiometers being compared are limited to the same latitudes. This means that when performing an inter-calibration of two radiometers with orbits of different inclination angle, data from the radiometer in the higher inclination orbit should be filtered to match the latitudes of the other radiometer.

#### IV. CONCLUSION

The double difference method for inter-calibration of microwave radiometers was presented and its performance assessed. The double difference method using the vicarious cold calibration is an effective method to inter-calibrate any two microwave radiometers, regardless of frequency, EIA, or

TABLE III

COMPARISON BETWEEN THE AMSR-E AND TMI DOUBLE DIFFERENCE SEASONAL CYCLE AMPLITUDE WITH LIMITING AMSR-E LATITUDES VERSUS USING ALL AMSR-E DATA. LIMITING THE AMSR-E LATITUDES RESULTS IN A SMALLER SEASONAL AMPLITUDE FOR ALL CHANNELS

Seasonal Cycle Amplitude (K)	10V	10H	19V	19H	22V	37V	37H
<i>DD limiting latitudes</i>	0.68	0.45	0.67	1.06	0.56	0.57	0.69
<i>DD all data</i>	0.76	0.89	1.01	1.60	1.36	0.63	1.29

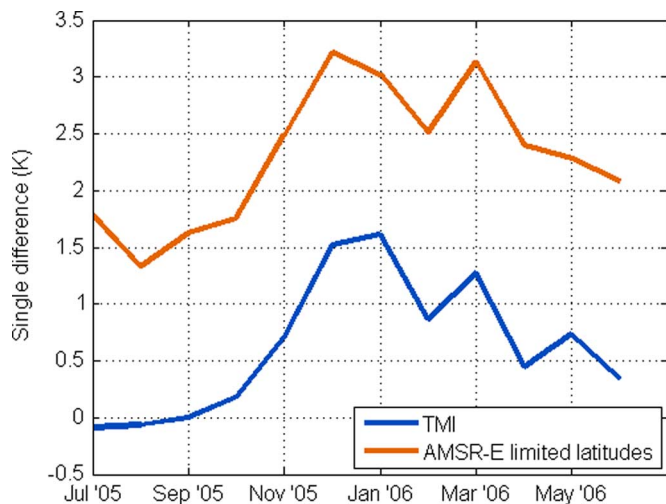


Fig. 10. Single difference for 22 V channel by month for TMI and AMSR-E using data with latitudes limited to TMI observed latitudes. Limiting the latitudes of AMSR-E produces a seasonal cycle in the single difference similar to TMI.

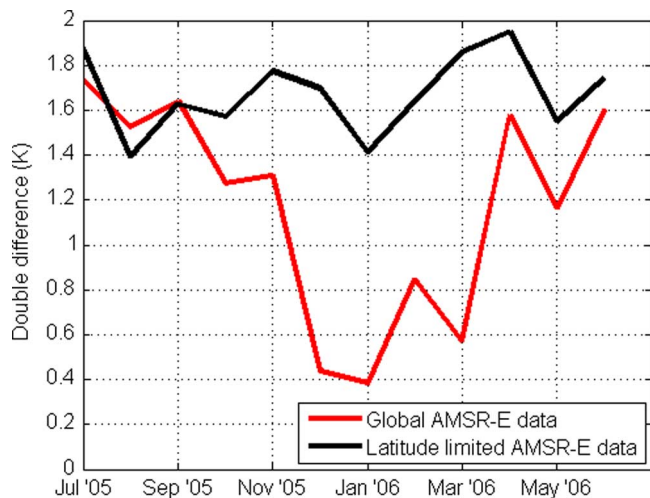


Fig. 11. Double difference AMSR-E—TMI using all AMSR-E data (globe) compared with using AMSR-E data with latitudes limited to TMI observed latitudes. Limiting the AMSR-E data to TMI latitudes decreases the seasonal cycle of the double difference.

orbit. The single difference was shown to greatly reduce the sensitivity to geophysical variability that is displayed in the cold cal TB by using simulated TBs to model a radiometer's observed TBs. The water vapor channel especially displays a seasonal cycle in the cold cal TB due to geophysical variation in the water vapor on Earth. The simulated TBs are necessary to reduce this large seasonal cycle. If the simulations are not

incorporated into the inter-calibration, such as is the case when using a direct comparison method, a large discrepancy can result due to frequency and EIA differences between the radiometers being compared. The single difference is also able to minimize scan biases arising from EIA difference across the scan in conical scanners due to attitude offsets. However, the single difference is not able to completely remove the seasonal cycle if the TB data set does not include all latitudes from the poles to the equator. As shown with TMI and AMSR-E data limited to TMI latitudes, the single difference displays a slight seasonal cycle, most apparent in the water vapor channel. This is most likely due to the simulations not being an accurate model of the observations. This error can be significantly reduced with the double difference, as long as the latitude ranges of the two radiometers being compared are the same.

## REFERENCES

- [1] M. C. Colton and G. A. Poe, "Intersensor calibration of DMSP SSM/I's: F-8 to F-14, 1987–1997," *IEEE Trans. Geosci. Remote Sens.*, vol. 37, no. 1, pp. 418–439, Jan. 1999.
- [2] C. Cao, M. Weinreb, and H. Xu, "Predicting simultaneous nadir overpasses among polar-orbiting meteorological satellites for the intersatellite calibration of radiometers," *J. Atmos. Ocean. Technol.*, vol. 21, no. 4, pp. 537–542, Apr. 2004.
- [3] B. Yan and F. Weng, "Intercalibration between special sensor microwave imager/sounder and special sensor microwave imager," *IEEE Trans. Geosci. Remote Sens.*, vol. 46, no. 4, pp. 984–995, Apr. 2008.
- [4] F. J. Wentz, P. Ashcroft, and C. Gentemann, "Post-launch calibration of the TRMM microwave imager," *IEEE Trans. Geosci. Remote Sens.*, vol. 39, no. 2, pp. 415–422, Feb. 2001.
- [5] P. W. Gaiser *et al.*, "The WindSat spaceborne polarimetric microwave radiometer: Sensor description and early orbit performance," *IEEE Trans. Geosci. Remote Sens.*, vol. 42, no. 11, pp. 2347–2361, Nov. 2004.
- [6] C. Kummerow, W. Barnes, T. Kozu, J. Shiue, and J. Simpson, "The tropical rainfall measuring mission (TRMM) sensor package," *J. Atmos. Ocean. Technol.*, vol. 15, no. 3, pp. 809–817, June 1998.
- [7] T. Kawanishi *et al.*, "The advanced microwave scanning radiometer for the earth observing system (AMSR-E), NASDA's contribution to the EOS for global energy and water cycle studies," *IEEE Trans. Geosci. Remote Sens.*, vol. 41, no. 2, pp. 184–194, Feb. 2003.
- [8] J. P. Hollinger, J. L. Peirce, and G. A. Poe, "SSM/I instrument evaluation," *IEEE Trans. Geosci. Remote Sens.*, vol. 28, no. 5, pp. 781–790, Sep. 1990.
- [9] A. Y. Hou, G. Skofronick-Jackson, C. D. Kummerow, and J. M. Shepherd, S. Michaelides, Ed., "Global precipitation measurement," in *Precipitation: Advances in Measurement, Estimation and Prediction*. New York: Springer, 2008, pp. 131–170.
- [10] D. McKague, C. Ruf, and J. Puckett, "Vicarious calibration of global precipitation measurement microwave radiometers," in *Proc. 2008 IEEE Int. Geoscience and Remote Sensing Symp., IGARSS*, 2008, pp. 459–462.
- [11] K. Gopalan, L. Jones, T. Kasparis, and T. Wilheit, "Inter-satellite radiometer calibration of WindSat, TMI, and SSM/I," in *Proc. 2008 IEEE Int. Geoscience and Remote Sensing Symp., IGARSS*, 2008, pp. 1216–1219.
- [12] T. Wilheit, W. Berg, L. Jones, R. Kroodsmas, D. McKague, C. Ruf, and M. Sapieno, "A consensus calibration based on TMI and WindSat," in *Proc. 2011 IEEE Int. Geoscience and Remote Sensing Symp., IGARSS*, 2011, pp. 2641–2644.

- [13] C. S. Ruf, "Detection of calibration drifts in spaceborne microwave radiometers using a vicarious cold reference," *IEEE Trans. Geosci. Remote Sens.*, vol. 38, no. 1, pp. 44–52, Jan. 2000.
- [14] U.S. National Centers for Environmental Prediction, Updated Daily: NCEP FNL Operational Model Global Tropospheric Analyses, Continuing From July 1999. Dataset ds083.2 Published by the CISL Data Support Section at the National Center for Atmospheric Research. Boulder, CO [Online]. Available: <http://dss.ucar.edu/datasets/ds083.2/>
- [15] T. Meissner and F. J. Wentz, "The complex dielectric constant of pure and sea water from microwave satellite observations," *IEEE Trans. Geosci. Remote Sens.*, vol. 42, no. 9, pp. 1836–1849, Sep. 2004.
- [16] J. Hollinger, "Passive microwave measurements of sea surface roughness," *IEEE Trans. Geosci. Electron.*, vol. 9, no. 3, pp. 165–169, Jul. 1971.
- [17] A. Stogryn, "The emissivity of sea foam at microwave frequencies," *J. Geophys. Res.*, vol. 77, no. 9, pp. 1659–1666, Mar. 1972.
- [18] T. Wilheit, "A model for the microwave emissivity of the ocean's surface as a function of wind speed," *IEEE Trans. Geosci. Electron.*, vol. GE-17, no. 4, pp. 244–249, Oct. 1979.
- [19] G. Elsaesser, "A parametric optimal estimation retrieval of the non-precipitating parameters over the global oceans," M.S. thesis, Colorado State Univ., Fort Collins, CO, 2006.
- [20] T. Meissner and F. J. Wentz, "An updated analysis of the ocean surface wind direction signal in passive microwave brightness temperatures," *IEEE Trans. Geosci. Remote Sens.*, vol. 40, no. 6, pp. 1230–1240, Jun. 2002.
- [21] P. W. Rosenkranz, "Water vapor microwave continuum absorption: A comparison of measurements and models," *Radio Sci.*, vol. 33, no. 4, pp. 919–928, 1998.
- [22] H. J. Liebe, G. A. Hufford, and T. Manabe, "A model for the complex permittivity of water at frequencies below 1 THz," *Int. J. Infr. Millim. Waves*, vol. 12, no. 7, pp. 659–675, 1991.
- [23] H. J. Liebe, P. W. Rosenkranz, and G. A. Hufford, "Atmospheric 60-GHz oxygen spectrum: New laboratory measurements and line parameters," *J. Quant. Spectrosc. Radiat. Transf.*, vol. 48, pp. 629–643, 1992.
- [24] D. S. McKague, C. S. Ruf, and J. J. Puckett, "Beam spoiling correction for spaceborne microwave radiometers using the two-point vicarious calibration method," *IEEE Trans. Geosci. Remote Sens.*, vol. 49, no. 1, pp. 21–27, Jan. 2011.



**Rachael A. Kroodsma** (S'09) received the B.S.E. degree in earth systems science and engineering from the University of Michigan, Ann Arbor, in 2009. She is currently working toward the Ph.D. degree in atmospheric and space science and the M.S.E. degree in electrical engineering at the University of Michigan, Ann Arbor.

Her research interests include development of calibration techniques for microwave radiometers, with an emphasis on inter-calibration of the radiometers for the Global Precipitation Measurement (GPM)

mission.



**Darren S. McKague** (M'08) received the Ph.D. degree in astrophysical, planetary, and atmospheric sciences from the University of Colorado, Boulder, in 2001.

He is an Assistant Research Scientist in the Department of Atmospheric, Oceanic and Space Sciences at the University of Michigan. Prior to working for Michigan, he worked as a systems engineer for Ball Aerospace and for Raytheon, and as a research scientist at Colorado State University. His work has focused on remote sensing with emphases on the development of space-borne microwave remote sensing hardware, passive microwave calibration techniques, and on mathematical inversion techniques for geophysical retrievals. His experience with remote sensing hardware includes systems engineering for several advanced passive and active instrument concepts and the design of the calibration subsystem on the Global Precipitation Mission (GPM) Microwave Imager (GMI) and the development of calibration techniques for the GPM constellation while at the University of Michigan. His algorithm experience includes the development of a near-real time algorithm for the joint retrieval of water vapor profiles, temperature profiles, cloud liquid water path, and surface emissivity for the Advanced Microwave Sounding Unit (AMSU) at Colorado State University, and the development of the precipitation rate, precipitation type, sea ice, and sea surface wind direction algorithms for the risk reduction phase of the Conical scanning Microwave Imager/Sounder (CMIS).

development of space-borne microwave remote sensing hardware, passive microwave calibration techniques, and on mathematical inversion techniques for geophysical retrievals. His experience with remote sensing hardware includes systems engineering for several advanced passive and active instrument concepts and the design of the calibration subsystem on the Global Precipitation Mission (GPM) Microwave Imager (GMI) and the development of calibration techniques for the GPM constellation while at the University of Michigan. His algorithm experience includes the development of a near-real time algorithm for the joint retrieval of water vapor profiles, temperature profiles, cloud liquid water path, and surface emissivity for the Advanced Microwave Sounding Unit (AMSU) at Colorado State University, and the development of the precipitation rate, precipitation type, sea ice, and sea surface wind direction algorithms for the risk reduction phase of the Conical scanning Microwave Imager/Sounder (CMIS).



**Christopher S. Ruf** (S'85–M'87–SM'92–F'01) received the B.A. degree in physics from Reed College, Portland, OR, and the Ph.D. degree in electrical and computer engineering from the University of Massachusetts, Amherst.

He is currently a Professor of atmospheric, oceanic, and space sciences; a Professor of electrical engineering and computer science; and Director of the Space Physics Research Laboratory, University of Michigan, Ann Arbor. He has worked previously at Intel Corporation, Hughes Space and

Communication, the NASA Jet Propulsion Laboratory, Pasadena, CA and Penn State University. In 2000, he was a Guest Professor with the Technical University of Denmark, Lyngby. He has published in the areas of microwave radiometer satellite calibration, sensor and technology development, and atmospheric, oceanic, land surface, and cryosphere geophysical retrieval algorithms.

Dr. Ruf is a member of the American Geophysical Union (AGU), the American Meteorological Society (AMS), and Commission F of the Union Radio Scientifique Internationale. He has served on the editorial boards of the AGU Radio Science, the IEEE TRANSACTIONS ON GEOSCIENCE AND REMOTE SENSING (TGRS), and the AMS JOURNAL OF ATMOSPHERIC AND OCEANIC TECHNOLOGY. He is currently the Editor-in-Chief of TGRS. He has been the recipient of three NASA Certificates of Recognition and four NASA Group Achievement Awards, as well as the 1997 TGRS Prize Paper Award, the 1999 IEEE Resnik Technical Field Award, and the 2006 International Geoscience and Remote Sensing Symposium Prize Paper Award.